Chapter 11

Raman Spectroscopy in Zinc Ferrites Nanoparticles

Pietro Galinetto, Benedetta Albini, Marcella Bini and Maria Cristina Mozzati

Additional information is available at the end of the chapter

http://dx.doi.org/10.5772/intechopen.72864

Abstract

$ZnFe_2O_4$ ferrite nanoparticles are arousing a great interest in the biomedical field, thanks to their superparamagnetic behavior at room temperature. Functional properties depend on composition, size, nanoparticle architecture and, in turn, on the synthesis methods. Bulk $ZnFe_2O_4$ has the normal spinel structure (all Zn^{2+} ions in tetrahedral and all Fe^{3+} ions in octahedral positions), but at the nanometric size inversion takes place with a cationic mixing on divalent and trivalent sites. The sensitivity of the Raman probe to cation disorder favored the appearance of several works on a rich variety of nanosized zinc ferrites. An overview on these results is reported and discussed at variance with synthesis methods, grain dimensions, and dopants. We add to this landscape our results from new nanosized powder samples made by microwave-assisted combustion, with different dopants (Ca, Sr on Zn site and Al, Gd on Fe site). A detailed analysis of A_{1g}, E_g, $3F_{2g}$ Raman modes has been performed and Raman band parameters have been derived from best-fitting procedures and carefully compared to literature data. The vibrational results are discussed taking into account the characterization from X-ray powder diffraction raction, SEM-EDS probe, EPR spectroscopy and, of course, the magnetic responses.

Keywords: zinc ferrites, nanostructures, Raman spectroscopy, cation disorder

1. Introduction

Zinc ferrite is a very popular material widely used at the nanometric size in different applicative fields [1–4]. $ZnFe_2O_4$ (ZFO) has a spinel structure and similarly to the whole ensemble of materials with the general formula MFe_2O_4 displays unique physical and chemical properties. In particular, zinc ferrite exhibits a peculiar mixing of high-quality functional properties. Indeed its magnetic, thermal, electrical, and mechanical properties coupled to a high chemical stability allowed its usage in magnetic storage, ferrofluids, catalysis, and biomedical applications, as for instance, theranostics and hyperthermia.

The spinel ferrite system can be written as $(Me_{1-x}Fe_x)^{2+}[Me_xFe_{2-x}]^{3+}O_4$ and contains two Fe^{3+} cations and a single divalent cation. The round and square brackets denote sites of tetrahedral (A) and octahedral [B] coordination, respectively, while x represents the degree of inversion defined as the fraction of the (A) sites occupied by Fe^{3+}. A completely inverse spinel is determined when the trivalent cations are equally distributed on tetrahedral and octahedral sites, while the divalent cations fill up the remaining half of the octahedral positions.

A very important characteristic of the spinel system is that it admits an extremely large variety of *total solid solutions*. The divalent cations are usually Zn^{2+}, Ni^{2+}, Mn^{2+}, Ba^{2+}, Cu^{2+}, but partial substitutions of divalent or trivalent Fe ions are possible, preserving the spinel crystal structure. When zinc enters to form bulk zinc ferrite the system assumes a normal spinel structure AB_2O_4: the oxygen atoms are arranged a network of close-packed face-centered cubic units; the divalent Zn cations (A) occupy tetrahedral sites and trivalent Fe cations (B) octahedral sites. Spinel unit cell is composed of 8 units builders. In the full unit cell, there are 8 Me^{+2}, 16 Fe^{+3} cations, and 32 anions oxide O^{-2} [1–4]. In **Figure 1**, a scheme of the direct spinel structure is reported.

The magnetic behavior of bulk ferrite system is strongly influenced by the nature, type, amount, and distribution of cations. Let us consider a deeply studied system, the mixed Zn-Ni ferrites ($Zn_{1-x}Ni_xFe_2O_4$, with $0 \leq x \leq 1$). The end compositions are zinc ferrite, $ZnFe_2O_4$ (for $x = 0$), i.e., a direct spinel, and nickel ferrite, $NiFe_2O_4$ ($x = 1$), an inverse spinel. In direct spinel $ZnFe_2O_4$, the behavior is antiferromagnetic with a Néel temperature about 9 K, while for nickel ferrite is ferrimagnetic with a Curie point about T = 860 K [5]. The possibility to control the chemical composition allows to finely tailor the magnetic features. These different behaviors can be understood looking at the magnetic interactions between B and A sites surrounding an oxygen [5].

In spinel ferrites, there are two sublattices: the tetrahedral one with one cation per formula and the octahedral one with two cations per formula. The magnetic behavior is determined by superexchange interactions between two transition cations separated by an oxygen. The A-O-B interactions have an axial symmetry, and thus are highly more efficient than the B-O-B

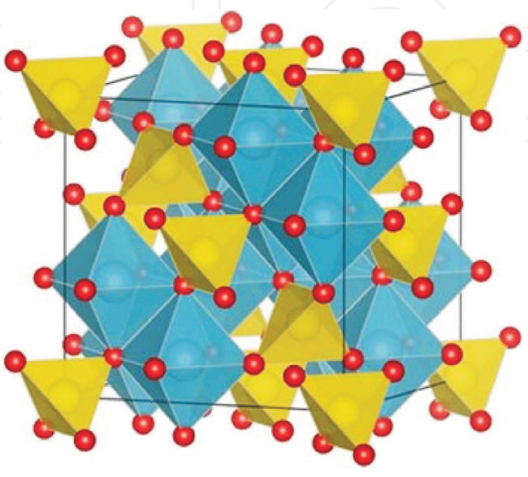

Figure 1. The direct spinel-type structure; the red circles represent oxygen ions while the ochre and cyan solids represent tetrahedral and octahedral units containing at the center Zn and Fe cations, respectively.

interactions, characterized by a 90° angle. As a result, both spins on B sites are antiparallel to the A spin. The magnetic response of spinel is thus determined by the cations distribution on A and B sites. In inverse $NiFe_2O_4$, B sites are occupied by both Ni^{2+} and Fe^{3+} ions and the remnant Fe^{3+} is placed on the A site. The magnetic moment of Fe^{3+} on A site cancels with the magnetic moment of Fe^{3+} on B site, and the resulting magnetic moment is the spin value for nickel Ni^{2+} (2.3 Bohr magnetons). This is a strong interaction with a resulting high-temperature Curie transition. In the case of zinc ferrite, iron ions occupy the B sites and zinc is located on the A site. Since Zn^{2+} is a $3d^{10}$ ion, it has no magnetic moment, and the only interaction is B-O-B, leading to an antiparallel arrangement of spins. The spins are identical, and the material becomes antiferromagnetic. The low Néel temperature clearly illustrates the weakness of this superexchange interaction, as compared with A-O-B of the nickel ferrite case [5].

The behavior of bulk spinel-type ferrites change markedly moving to the nanoscale regime. In particular, the insurgence of a superparamagnetic (SPM) behavior at room temperature (RT) has been observed [6]. In systems that are ferro- and ferrimagnetic in bulk, SPM state can appear when the grain size is reduced to 50 nm or less. In SPM phase, the thermal energy k_BT is greater than the magnetic anisotropy energy, and therefore random fluctuations of the magnetization are possible. The magnetization of a SPM material, above the so-called blocking temperature (T_B), is equal to zero in the absence of an external field, and it rapidly increases under application of an external field. This fact implies a closed sigmoidal shape of the M-H curve without appreciable hysteresis. Experimentally, the value of T_B typically corresponds to the "merging point" of the zero-field cooled (ZFC) and field-cooled (FC) magnetization curves [5].

SPM is not the only magnetic phenomenon caused by the finite size effect of nanoparticles. The reduction in size and the increase of the surface/volume ratio can, for example, produce randomly oriented uncompensated surface spins, canted spins, and magnetically dead layer at the surface [7].

Anyways, superparamagnetism is especially important in applications such as drug delivery or MRI, where the nanoparticles exhibit no magnetic properties upon removal of the external field and therefore have no attraction for each other, eliminating the major driving force for aggregation. More importantly, superparamagnetic nanoparticles allow better control over the application of their magnetic properties because they provide a strong response to an external magnetic field.

For biomedical application, it is thus essential to finely control the functional parameters: saturation magnetization (M_s), coercivity (H_c), and blocking temperature (T_B). This control can be made by tailoring the material properties in terms of size, shape, composition (substitutions, doping, cation distribution in the crystal structure), and shell-core design, with possible different chemical and physical structures of internal-core and surface-shell parts of the nanoparticle [7].

A large number of synthesis methods were reported, including conventional ceramic solid state synthesis, high-energy ball milling, microwave-assisted combustion, sol-gel, hydrothermal, co-precipitation, ultrasonic cavitation, and thermal plasma, with the peculiar aim to tune electric, catalytic, and magnetic properties, these last ones particularly appealing for biomedical application [8]. In the following, the most widespread synthesis methods for ferrites will be briefly described.

1.1. Conventional ceramic method

The conventional solid-state reaction, starting from metal oxides or carbonates, is the oldest method for the synthesis of ceramics, since it is economic, efficient, and easily scalable. In fact, despite of some disadvantages, such as particle agglomeration and growth, it is still regularly used to synthesize novel materials for the first time, also for the widespread diffusion of the necessary equipment in academic laboratories.

1.2. High energy ball milling

The use of mechanical milling in the preparation of inorganic materials (ceramics, metals, and alloys) has a long tradition. It is a cheap and relatively rapid method that, in some cases, guarantees the formation of the desired compounds without the need of other thermal treatment. The tuning of ferrites nanoparticles could be obtained by changing milling container, speed, time, ball-to-powder weight ratio, extent of filling the vial, milling atmosphere, presence of a process control agent, temperature of milling, etc. [9].

1.3. Microwave combustion method

This method is actually one of the most diffused due to its numerous advantages: is a wet chemical technique, enables fast reaction rate, chemical homogeneity, and high reactivity due to the uniform heating produced by microwaves. Some drawbacks are represented by the difficulty to vary the spherical form of particles and to control the valence states of the elements [10].

1.4. Sol-gel method

The sol-gel technique is a wet low-temperature method that provides products with a perfect chemical composition and takes advantages over the others, owing to good stoichiometric control and homogeneity, short preparation time and inexpensive precursors. Furthermore, it provides nanoparticles with controlled sizes and defined morphology. Generally, for the production of multicomponent oxides, alkoxides (substituted in some cases by acetates) are put together in alcohol. In the sol-gel method water, alcohol, pH, concentration of alkoxides, and controlled temperature are required for proper hydrolysis [11].

1.5. Hydrothermal method

The hydrothermal route is a convenient wet way to produce well crystalline materials, with particles with suitably tuned size and shape. The main advantage of hydrothermal synthesis over conventional wet-chemistry methods is that it occurs under non-standard conditions, and that non-classical crystallization pathways can be explored. Many factors can be varied such as temperature, reagents ratio, solvents, and kind of salts to customize the ferrite nanoparticles [12].

1.6. Co-precipitation method

This method is probably the most favorable to produce nanoparticles, as well as simple and very productive. A high homogeneity and uniformity can be easily obtained at moderate

experimental conditions. In these last years, this kind of synthesis has been mainly used to produce nanoparticles with peculiar magnetic properties, in particular superparamagnetism for biomedical application. The particle growth is controlled only by kinetic factors, so by controlling pH, temperature, ionic strength, salts nature or the Fe(II)/Fe(III) concentration ratio, the shape and size of the nanoparticles can be customized [13].

1.7. Green synthesis

Recently, plant-based green syntheses of nanoparticles have attracted the attention of researchers. Various green resources, like micro-organisms and plants, are available for these syntheses. The extract of plants not only acts as reducing agent toward the metal ions in a short time with respect to micro-organisms or the classical organic/inorganic substances, but also provides high-yield nanosized particles. The preparation time of nanoparticles depends upon the variety of plants and the concentration of phyto-chemicals. Plant-based green synthesis of magnetic nanoparticles is still under research [14, 15].

Among the so-called physical methods, the most used to produce zinc ferrites are the following.

1.8. Ultrasonic cavitation method

Ultrasonic cavitation chemistry is useful for synthesizing a variety of compounds at milder conditions. The major advantage of this method is that it affords a reliable and facile route for the control of both the synthetic process and nanostructure of advanced materials. This process also provides chemical homogeneity and reactivity through atomic level mixing and phase pure crystalline materials can be prepared by annealing at reduced temperatures. In addition, the use of additive components (stabilizers or surfactants, precipitants) and particular calcination requirements are avoided [16].

1.9. Thermal plasma

Thermal plasmas, such as direct current arcs and radio frequency (RF) plasmas, offer unique advantages for the synthesis of ceramic powders due to the easily achievable high temperatures and energy densities. In a RF thermal plasma flame, the gas temperatures may exceed 10^4 K independently of the gas composition. In addition, a high temperature gradient exists between the hot plasma flame and the surrounding gas phase. The resulting rapid quenching rate is favorable for producing fine particles with unstable structures in thermodynamic terms [17].

The large variety of methods used to obtain zinc ferrites nanoparticles reflects on a very scattered scenery in terms of properties of the obtained materials. This is not simply due to the above-mentioned close correlation among functional parameters and morphology, gran size, intentional doping, cation distribution, and nanoparticle architecture. Indeed, it is extremely important to verify and control the magnetic, structural and chemical purity, and homogeneity of nanoparticles because even low amount of extrinsic phases or elements can alter the functional properties. In particular, it is very important to monitor the presence of unwanted iron oxides phases, possible source of extrinsic contribution to the functional properties of zinc

ferrites. In addition, several factors such as nucleation, growth, aggregation, and adsorption of impurities can affect the morphology of prepared particles [18]. It is thus evident the need to deeply characterize the materials with a multi-technique approach to reveal even subtle effects due to unwanted alterations of the designed nanoparticles.

Usually, all the researchers give evidence of the magnetic properties measuring by SQUID magnetometer or Vibrating Sample Magnetometry, Saturation magnetization (M_s), Coercivity (H_c), and Blocking temperature (T_B). The local inspection about the source of magnetic behavior is usually accomplished by combining ^{57}Fe Mossbauer, XANES, XPS, and EPR investigations. Morphology and chemical compositions are usually investigated by TEM and SEM techniques, the latter with the possibility to perform EDX analyses for elemental check. Sometimes, LA-ICP is used to validate the composition. Crystalline structure quality is usually assessed by XRD analyses and micro-Raman measurements, that also allowed to estimate the inversion degree.

Raman spectroscopy (RS) has been widely used to study spinel ferrites and in particular zinc ferrites both for routine identification of materials [19] and for very fine investigations concerning basic phenomena. This is due to an interesting overlapping between characteristics of RS and properties of nanosized zinc ferrites: (i) RS sensitivity to cations distribution [20], (ii) RS ability to reveal the presence of extrinsic iron oxides phases like hematite or magnetite [21], (iii) possibility to use RS to monitor stability of spinel ferrites vs. light exposure or thermal treatment [22], (iv) influence of nanometric scaling on Raman lines features—peak energies, widths and shape [23], (v) possibility to evaluate the presence of unwanted impurities. In addition, it is important to note that Raman spectroscopy has been used to study Surface-enhanced Raman scattering (SERS) when ferrites nanoparticles are functionalized for specific biomedical applications [24].

In this chapter, we combine a brief overview on the literature about Raman data from different zinc ferrites nanoparticles to new Raman results by our group on pure and doped zinc ferrites nanoparticles prepared by using the microwave-assisted combustion method. In particular, we present data obtained from undoped $ZnFe_2O_4$, $Zn_{1-x}Ca_xFe_2O_4$ (x = 0.05 and 0.25), $ZnFe_{1.9}Gd_{0.1}O_4$, $Zn_{0.95}Sr_{0.05}Fe_2O_4$, and $ZnFe_{1.9}Al_{0.1}O_4$ doped ferrites. The Ca substitution is particularly interesting due to the low toxicity of the substituent; on the other side, Gd ions are commonly used as contrast agents for MRI. In all the cases, the Raman data are accompanied by recalling functional parameters and synthesis procedures. For our samples, a more complete description about synthesis, morphology, and magnetic behavior are outlined allowing a better comprehension about the powerful of Raman spectroscopy in this kind of system.

2. Raman effect in $ZnFe_2O_4$ nanoparticles

$ZnFe_2O_4$ spinel has a cubic structure that belongs to the space group Fd3m (O^7_h) consisting of 8 molecules within the unit cell, for a total of 56 atoms; nevertheless the smallest Bravais

cell contains 2 formula units for a total of 14 atoms. By the factor group analysis, it is possible to derive the following 42 modes in $ZnFe_2O_4$ spinel, 3 acoustic modes, and 39 optical modes [19]:

$$A_{1g}(R) + E_g(R) + F_{1g} + 3F_{2g}(R) + 2A_{2u} + 2E_u + 4F_{1u}(\text{IR}) + 2F_{2u} \quad (1)$$

where the (R) and (IR) identify Raman-active and infrared-active vibrational species, respectively, and the rest of the modes are silent modes. The $E_{g,u}$ and $F_{1g,2g,1u,2u}$ modes are doubly and triply degenerate, respectively. The three acoustic modes belong to the F_{1u} species.

Thus in the Raman spectra of zinc ferrites, only five modes $A_{1g} + E_g + 3F_{2g}$ should be observed [25]. The three Raman-active F_{2g} modes are labeled $F_{2g}(1)$, $F_{2g}(2)$, and $F_{2g}(3)$, where $F_{2g}(1)$ is the lowest frequency F_{2g} mode and $F_{2g}(3)$ is the highest frequency mode of this vibrational species.

Figure 2 shows the spectra from two different ZFO prepared by our group. These spectra are reported as an example of the features detected in the Raman spectrum of ZFO. The red spectrum is obtained from pure ZFO, synthesized by solid state reaction (see Section 2.2.), while the black curve is the Raman signal of an Al-doped ZFO sample synthesized by co-precipitation method. In the region 100–800 cm^{-1}, three different spectral intervals can be recognized for both samples: (i) 600–800 cm^{-1} is the region of A_{1g} modes; (ii) 410–550 cm^{-1} is the region of $F_{2g}(3)$ modes, and (iii) 260–380 cm^{-1} should be the region of $F_{2g}(2)$ modes. At lower frequencies, E_g and $F_{2g}(1)$ are sometimes detected. Furthermore in the spectrum from Al-doped sample, narrow extra peaks are detected at about 218, 285, and 395 cm^{-1}. These

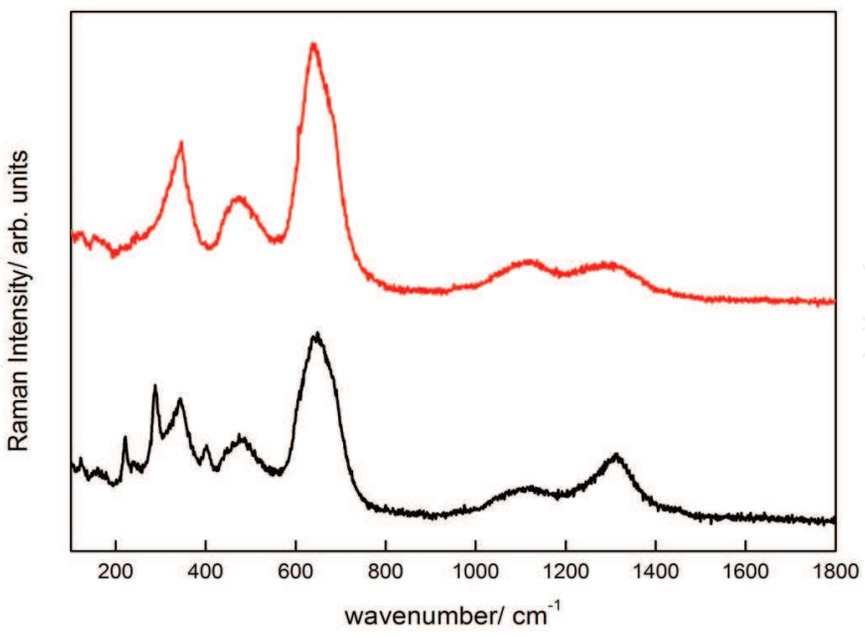

Figure 2. Raman spectra from two different ZFO prepared by our group: Pure ZFO synthesized by solid state reaction (red curve) and Al-doped ZFO synthesized by conventional co-precipitation method (black curve). The latter will not be further considered in the chapter.

Raman lines are associated to the presence of hematite inside the irradiated volume [21]. At higher energies, in the region 1000–1800 cm^{-1} only second-order features can be revealed, with a more intense feature just above 1300 cm^{-1} in the Al-doped sample due to second-order signal from hematite.

Briefly, we recall that micro-Raman measurements were carried out at RT by using a Labram Dilor spectrometer equipped with an Olympus microscope HS BX40. The 632.8 nm light from He-Ne laser was employed as excitation radiation. The samples, mounted on a motorized *xy* stage, were tested with a 100× objective and with a laser spot of 1 μm of diameter. The spectral resolution was about 1 cm^{-1}. Neutral filters with different optical density were used to irradiate the samples at different light intensities leading to power density values from 5×10^3 to 5×10^5 W/cm^2. A cooled CCD camera was used as a detector and the typical integration times were about 2 min. The sample phase homogeneity was verified by mapping the Raman spectra from different regions of each sample. The parameters of the Raman spectra were extracted by using best fitting procedures based on Lorentzian functions. In this way, the frequency, full width at half maximum, intensity, and integrated intensity of the peaks were determined.

2.1. Brief overview from the literature

Even if in the literature the assignment of the specific atomic motions within the spinel lattice during the Raman-active vibrations is controversial, it is common to explain the vibrational dynamic in term of normal modes inside the two sub-units within the spinel unit cell: the tetrahedral unit, AO_4 is comprised of the cation at the center of a cube and four oxygen atoms in the nonadjacent corners; the octahedral unit consists of a cation surrounded by six oxygen atoms, two along each dimensional axis, to form a BO_6 octahedron. It is accepted that the highest-frequency A_{1g} mode is assigned to the symmetric breathing mode of the AO_4 unit within the spinel lattice [26]. The oxygen atoms move away from the tetrahedral cations along the direction of the bonds, with all the cations at rest. For all the other Raman modes, there are some controversies about their assignments. In [27], all the other low frequency modes are attributed to vibrations inside the octahedral sites (BO_6). Besides the highest-frequency Raman-active $F_{2g}(3)$ mode is alternatively attributed to the antisymmetric breathing of the AO_4 unit [28], or to the asymmetric bending motion of the oxygens bonded to the tetrahedral cations [29].

The $F_{2g}(2)$ mode should be due to the opposite motion of cation and oxygen along one direction of the lattice [30]. In [30], the E_g mode is assigned to the symmetric bending motion of the oxygen anions within the AO_4 unit, in agreement to other researchers [28]. Finally, more agreement is found for $F_{2g}(1)$ Raman mode, the lowest frequency one, due to the complete translation of the AO_4 unit within the spinel lattice [31–34].

The controversial landscape of Raman modes in ZFO is summarized in **Table 1**, where we report a brief overview on Raman results from nanosized pure zinc ferrites obtained by different methods.

Method	Average size (nm)	Main Raman modes peak energy (cm^{-1})						References
		$F_{2g}(1)$	E_g	$F_{2g}(2)$	$F_{2g}(3)$	A_{1g} (1)	Other signals	
S MC	3–25	150	265	350–400	450–500	630 (Zn-O) 720 (Fe-O)	—	[35, 36]
Honey-mediated SG C	10–20	241	351	498	438	605 (Zn-O) 653 (Fe-O)	221, 286, 403 α-Fe_2O_3	[37]
S MC	20	160	265	370	450	637(Zn-O) 670(Fe-O)	721 A_{1g} maghemite	[38]
TD	4.7	159	254	364	459	665	—	[39]
CG	13	—	351	452	490	650 (Zn-O) 700 (Fe-O)	—	[40]
CP	5	—	330	480	—	660	—	[41]
SG AC	21	262	357	497	—	682	—	[42]
SG C	19.6	174.9	340.3	491	—	652.7 688.6	—	[43]
HT F	—	221	246	355	451	647	800 noise	[27]
CP	7	235.56	339.61	487.4	—	664.97	—	[23]

The data are listed at variance with synthesis method and grain size. For syntheses, we used the following acronyms: S MC for soft mechanochemical, SG C for sol-gel combustion, TD for thermal decomposition, CG for citrate-gel, CP for co-precipitation, SG AC for sol-gel autocombustion and HT F for high temperature flux.

Table 1. Overview on data from literature on Raman modes in pure ZFO nanoparticles.

At first, one can notice the absence of a clear correlation between grain size and peak positions of A_{1g} modes. Looking at the spectra, the effect of grain size reduction causes as expected an asymmetric broadening of Raman bands and a decreasing of Raman intensities [44, 45]. A_{1g} mode is mainly the most intense Raman feature; while in [27, 37, 46], the highest Raman signal is the Eg mode. Besides, in ZFO, the nanometric regime is primarily the cause of inversion, with marked influence on Raman spectra. Indeed in tetrahedra and octahedra a mixing between A and B cations takes place and this mixing reflects on Raman modes due to different cations involved for the same vibrational modes [35].

In **Table 2**, we summarize some results from nanocrystalline doped zinc ferrites and other common ferrites.

Both for pure and doped nanoparticles zinc ferrites, it is difficult to derive general rules for Raman modes behavior. Different parameters (synthesis, grain size, composition, and chemical purity) can give rise to competing effects with opposite effects on Raman features. In addition, it is evident from the reported data in **Tables 1** and **2** that even the attribution of a certain Raman signal to a specific mode is uncertain, in particular for F_{2g} and E_g modes. Furthermore for F_{2g} and E_g modes, the analyses are complicated by the usually lower intensities. Recently, even the attribution of A_{1g} mode has been reconsidered. Some authors [50, 51] claimed that

Sample	Method/ SynthesIs	Average size (nm)	Main Raman modes peak energy (cm^{-1})						References
			$F_{2g}(1)$	E_g	$F_{2g}(2)$	$F_{2g}(3)$	A_{1g} (1)	Other signals	
$ZnFe_{1.8}La_{0.2}O_4$	SG AC	10	250	343	487	—	663	—	[42]
$Ni_{0.5}Zn_{0.5}Fe_2O_4$	S MC	20	125 (Zn-O)	256 (Zn-O)	362 (Zn)	370 (Zn)	637(Zn-O)	721	[38, 47]
			200 (Ni-O)	323 (Ni-O)	480 (Ni)	480 (Ni)	670(Fe-O)	A_{1g} maghemite	
							689(Ni-O)		
$Mn_{0.45}Ni_{0.05}Zn_{0.5}Fe_2O_4$	C	9	—	336	482	540	636 (Zn-O)	—	[48]
							680 (Fe-O)		
$Mn_{0.05}Ni_{0.45}Zn_{0.5}Fe_2O_4$	C	12	—	339	484	550	650 (Zn-O)	—	[48]
							695 (Fe-O)		
$Mn_{0.65}Zn_{0.35}Fe_2O_4$	CG	9	—	350	—	540	610 (Mn-O)	—	[40]
							650 (Zn-O)		
							690 (Fe-O)		
$Mn_{0.6}Zn_{0.4}Fe_2O_4$	SG C	9.4	217.7	275.3	386.5	490.8	591.3	240, 300	[43]
							645.7	α-Fe_2O_3	
$Co_{0.5}Zn_{0.5}Fe_2O_4$	CP	—	207.7	314.5	468.5	551.7	632.7 A_{1g} (1)	—	[49]
							693.2 A_{1g} (2)		
$NiFe_2O_4$	S MC	10	188	323	480	550	670 (Fe-O)	721	[38]
							689 (Ni-O)	A_{1g} maghemite	
$CoFe_2O_4$	DM	6	547.7	293.2	460.7	190.2	674.8 A_{1g} (1)	—	[20]
							604.9 A_{1g} (2)		
$MnFe_2O_4$	SG C	8.5	220.6	277	370.9	507.4	593	240, 300	[43]
							638.7	α-Fe2O3	
$FeFe_2O_4$	TD	4.9	190	290	453	535	671	720, 604, 496, 386 maghemite	[39]

The data are listed at variance with synthesis method and grain size. For the acronyms, see the caption of **Table 1**. In addition, C stays for citrate and DM for double microemulsion.

Table 2. Overview on data from literature on Raman modes in doped ZFO nanoparticles.

the Raman band at around 650 cm^{-1} is associated with the presence of Zn^{2+} ions at B-sites. This conclusion seemed to be supported by the dependence of its intensity with Zn content in $Mg_{1-x}Zn_xFe_2O_4$ and by Mossbauer data. Nevertheless, some common features can be derived: the mass of the tetrahedral cations is effective in the A_{1g} lineshape with different contribution clearly detectable, as expected in a simple "mass on a spring" model; the reduced grain size causes a decrease in the total Raman yield; all the synthesis methods seem to be able to produce nanoparticles with good crystallinity even if sometimes the Raman signals are quite weak and broadened [22, 52]. Further worsening in the quality of Raman spectra has been observed when ZFO NP is functionalized for specific biomedical applications [53].

In the Raman spectra of nanocrystalline, both pure and doped zinc ferrites or other ferrites, it is common to recognize different contributions for each Raman mode, just due to different cations involved in a specific vibration [47]. This behavior, the so-called *two-mode* behavior, is particularly evident for the most intense A_{1g} mode above 600 cm^{-1}. If doping is considered, the Raman lineshape is affected both by the inversion on A and B sites and by the substitution of divalent or trivalent cations. Thus, the Raman signal in the more complex case could be the result of the overlapping of three contributions due to vibrations inside (i) ZnO_4, (ii) FeO_4, due to inversion, and (iii) the MeO_4 due to substitution. The two mode behavior is sometimes less detectable in the lower frequency modes; where in some cases, a one-mode behavior cannot be excluded [54]. The Raman studies on ZFO NP have usually the goal to characterize the structure of the samples in view of the magnetic response, being the last affected by inversion and/or cationic substitutions with magnetic ions. Raman data, and in particular the A_{1g} modes, are usually used to perform best-fitting analyses using lorenztian curves and derive the integrated intensities of the two (or three if substituents are considered) different contributions. With the empirical formula $x_{Fe}(A) = [1 - I_{Zn}/(I_{Zn} + I_{Fe})]$, one can derive the inversion degree; the lorentzian intensities

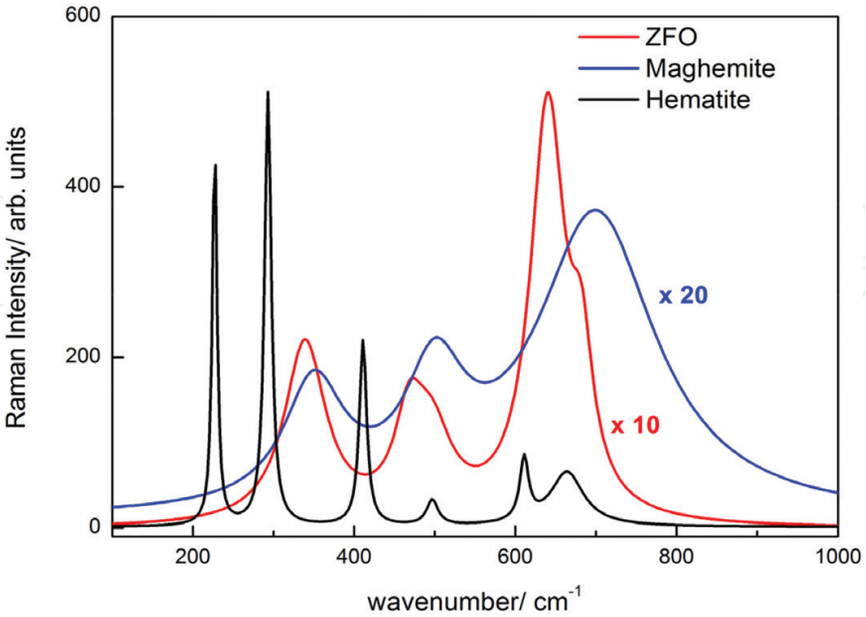

Figure 3. Simulated Raman spectra for ZFO, hematite and maghemite. The intensities are scaled to match the experimental evidences on pure micrometric powders.

can be multiplied by corresponding force constants even if it is not simply to derive a reliable value [39, 47].

For this reason, an important issue in ZFO NP studies is to reveal in synthesized samples the presence of iron oxides, like hematite and maghemite [5]. These oxides can infer an effective but extrinsic magnetic behavior with problems in terms of stability and aggregation if used in biomedical applications. To characterize the spin ordering and understand the nature of magnetic behavior, Mossbauer and neutron diffraction studies have been helpfully used [55]. Nevertheless, in this frame also the Raman spectroscopy can play an important role. Hematite (α-Fe_2O_3) belongs to the rhombohedral system while maghemite (γ-Fe_2O_3) has a cubic inverted spinel structure, thus from the point of view of Raman activity equivalent to ZFO. These differences reflect on the Raman spectra. In **Figure 3**, we report the simulated spectra for ZFO, hematite, and maghemite.

The Raman spectra of ZFO and maghemite are obviously quite similar with a total Raman yield greater for the former. The main difference is the peak position of the A_{1g}. In ZFO, the ZnO_4 vibrations are dominant and the peak is around 650 cm^{-1}, while in maghemite only the iron is present and the energy peak is usually observed around or just above 700 cm^{-1}. On the contrary, the Raman spectrum of hematite is markedly different having the main peaks in the lower energy region. It is important to note that the Raman yield of hematite is approximately 10–20 times higher than that of spinel-type ferrites, thus a small amount of hematite is enough to give clear signatures in Raman spectrum. It is difficult to quantify this small amount because it is often reported that for ZFO nanometric grains, surface shell of hematite or maghemite can be formed [37, 56]. In this case, the surface sensitivity of the Raman technique can hinder a proper estimation. A more difficult goal is to reveal the presence of few amounts of maghemite in ZFO by Raman spectroscopy. Detailed best-fitting analyses are usually performed on the A_{1g} data, and it is possible to infer about the presence of maghemite [38]; but the variability of peak energies found both for pure and doped ZFO and the weak weight of maghemite contribution in Raman signal hinder a reliable attribution simply based on Raman data. But, RS allows to monitor the stability of maghemite to laser irradiation. Indeed, it is well-known that in the oxidation route of iron ions maghemite is an intermediate metastable phase while hematite is the terminal and stable one [57]. Using this approach, the presence of maghemite in ZFO can be indirectly evaluated by the insurgence of hematite Raman signals under laser irradiation [58].

2.2. Experiments from pure and doped zinc ferrites obtained by microwave-assisted combustion method

We focused on the microwave combustion synthesis method of Ca (on Zn site) and Gd (on Fe site) substituted ferrites. Undoped $ZnFe_2O_4$ and Sr, and Al doped samples were also synthesized and used for comparison. All the samples have been investigated by X-ray powder diffraction and SEM-EDX analyses as a complement of Raman results. The magnetic behavior has been measured by SQUID magnetometry. All the experimental details are reported elsewhere [59].

We found, for all the samples, a superparamagnetic behavior with saturation magnetization between 6 and 10 emu/g at the maximum applied magnetic field of 3 T, with a more effective role played by Ca ions with respect to Gd ions substitution.

2.2.1. Synthesis

The samples were synthesized by microwave-assisted combustion methodology (MW), a rapid and green method as previously described, and by a conventional high energy ball milling.

For MW, the starting reagents were $Zn(NO_3)_2$ $6H_2O$ and $Fe(NO_3)_3$ $9H_2O$ taken in stoichiometric ratio to obtain $ZnFe_2O_4$ and mixed in an agate mortar with a proper amount of citric acid as fuel, as calculated from the propellant chemistry theory [60]. In brief, by taking into account the reducing and oxidizing valences of the involved elements (Zn = +2, N = 0, O = −2, Fe = +3, C = 4, H = 1), we can calculate a global valence value of −15, −10, and +18 for iron nitrate, zinc nitrate, and citric acid, respectively. We can write the balanced chemical reaction for the ferrite formation as $2\cdot(-15) + 1\cdot(-10) + x\cdot(+18) = 0$ and the mol amount of citric acid necessary to reduce the nitrates oxidant amount is calculated as 2.22.

The mixture was placed in a ceramic crucible in a microwave oven for 30 min at 800 W: this power ensures a temperature inside the oven between 450 and 500°C. This undoped sample will be named ZnFe. To obtain the doped samples, proper amount of $Ca(NO_3)_2$ $4H_2O$, $Sr.(NO_3)_2$, $Gd(NO_3)_3$ $6H_2O$, and $Al(NO_3)_3$ $9H_2O$ were added to the previous reagents to obtain the desired stoichiometry $Zn_{0.95}Ca_{0.05}Fe_2O_4$, $Zn_{0.75}Ca_{0.25}Fe_2O_4$, $Zn_{0.95}Sr_{0.05}Fe_2O_4$, $ZnFe_{1.9}Gd_{0.1}O_4$, and $ZnFe_{1.9}Al_{0.1}O_4$. The citric acid amount to add to the various mixtures was calculated as explained. In the following, these samples will be named Ca005, Ca025, Sr005, Gd01, and Al01, respectively.

For comparison, an undoped $ZnFe_2O_4$ sample was also synthesized by means of a classical solid-state synthesis, starting from a stoichiometric mixture of ZnO and Fe_3O_4 oxides ground by ball milling in tungsten jars for 6 h at 500 rpm with intermediate periods of last. The mixture was then treated in oven in air at 650°C for 12 h (heating rate 5°C/min, spontaneous cooling to 25°C) and ground after cooling. This sample will be named ZnFe-SS.

2.2.2. XRD and SEM analyses

X-ray diffraction analysis was used to determine the sample purity, in particular to control the effective cation substitution, the crystallite sizes and the eventual inversion degree of the spinel by means of the structural and profile refinement based on the Rietveld method. In **Figure 4**, the XRD patterns of the ZnFe-SS and ZnFe undoped $ZnFe_2O_4$ samples are shown together with Ca005 one. In all the cases, a pure ferrite sample is formed, whose peaks well agree with the $ZnFe_2O_4$ cubic spinel structure (PDF card N. 89-7412). It is well evident a different peaks broadening and crystallinity between MW and SS samples suggesting markedly different particle sizes, as can be expected due to the different experimental synthesis methodologies. For the doped samples, XRD patterns demonstrate that the doping successfully occurred, because neither traces of unreacted reagents nor phase impurities are present: only for Sr005, some low peaks reveal the presence of small traces of strontium nitrate, as a residual of the reagent. The structural refinement on the basis of the Rietveld method was performed on all the patterns by using the known cubic spinel model: the main refined structural parameters are reported in **Table 3**. It can be seen that the crystallite sizes are in the nanometer range: the values for the microwave synthesis are all lower than 11 nm, while for ZnFe-SS a value of 22 nm is found.

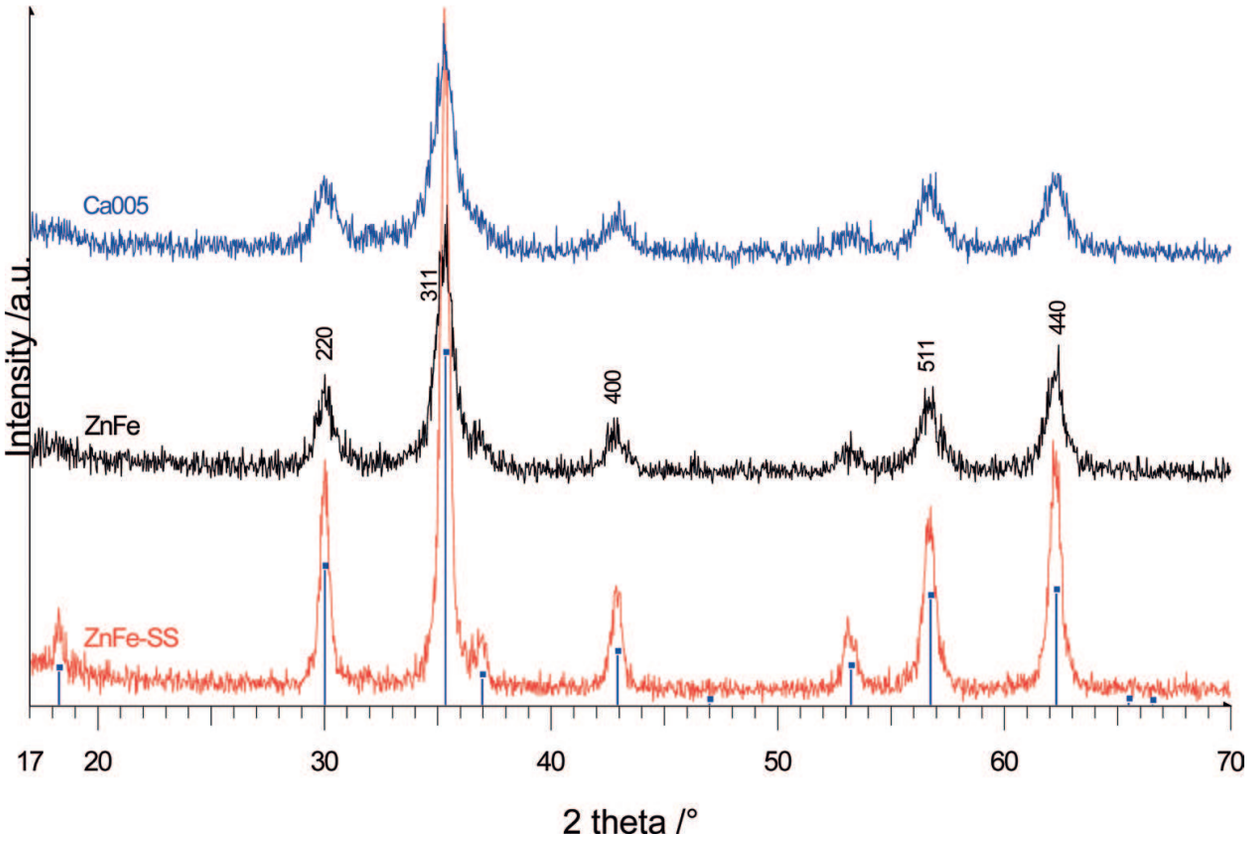

Figure 4. XRD patterns of undoped $ZnFe_2O_4$ obtained from microwave combustion and solid state methods together with the Ca005 pattern. The bars of the expected angular positions of the spinel phase (JCPDS card 89–7412) are also reported, together with the miller indices of the main peaks.

	Cations distribution	Impurities	a/Å	Size/nm
ZnFe-SS	$[Zn_{0.93}Fe_{0.07}]_T[Fe_{1.93}Zn_{0.07}]_O$	—	8.4386(6)	22.9
ZnFe	$[Zn_{0.82}Fe_{0.18}]_T[Fe_{1.82}Zn_{0.18}]_O$	—	8.4371(40)	11.1
Al01	$[Zn_{0.68}Fe_{0.32}]_T[Fe_{1.58}Al_{0.1}Zn_{0.32}]_O$	—	8.4221(25)	8.4
Ca005	$[Zn_{0.90}Ca_{0.05}Fe_{0.05}]_T[Fe_{1.95}Zn_{0.05}]_O$	—	8.4343(17)	8.7
Ca025	$[Zn_{0.21}Ca_{0.25}Fe_{0.54}]_T[Fe_{1.46}Zn_{0.54}]_O$	—	8.4331(57)	5.5
Sr005	$[Zn_{0.88}Sr_{0.05}Fe_{0.07}]_T[Fe_{1.93}Zn_{0.07}]_O$	$Sr(NO_3)_2$ 3.35	8.4380(13)	7.2
Gd01	$[Zn_{0.98}Fe_{0.02}]_T[Fe_{1.88}Gd_{0.1}Zn_{0.02}]_O$	—	8.4366(29)	8.4

Table 3. Cation distribution, impurity phases amount, lattice parameter, and crystallite size as derived from XRD analyses.

The lattice parameters although may vary due to the different ionic radii of the dopants with respect to Zn and Fe ions, are quite similar. On the other hand, a similar behavior for the lattice parameter was found for the Sr substituted samples [10]. Only for Al doping the cubic parameter decreases with respect to the undoped sample: in fact, a value of 0.53 Å is reported for Al^{3+} ions radius with respect to 0.65 Å of Fe^{3+} in high spin configuration [61]. The inversion degree, i.e., the amount of Fe ions on Zn crystallographic sites, was also determined from the structural

refinement. In all the cases, the inversion takes place, although not so markedly: only for Ca025 a value of 0.54 is reached. The easily induced inversion can be a consequence of the quickness of the MW synthesis that in only about 30 min can produce a good level of crystallinity but with atomic disorder. We also verified that Ca and Sr. ions seem to prefer the A site, while Al and Gd ions the B one. This is certainly true when the substitution is about 5 atom%, while for Ca025 a different model could be hypothesized. In fact, due to the preference of calcium for octahedral coordination it is possible that these ions could be also located on Fe sites, so inducing a higher inversion degree with respect to Ca005 and a small contraction of the lattice parameter.

In **Figure 5a,b**, SEM images of Gd01 and ZnFe-SS clear up the morphological differences between the samples from MW synthesis and solid state, giving evidence of a higher surface/

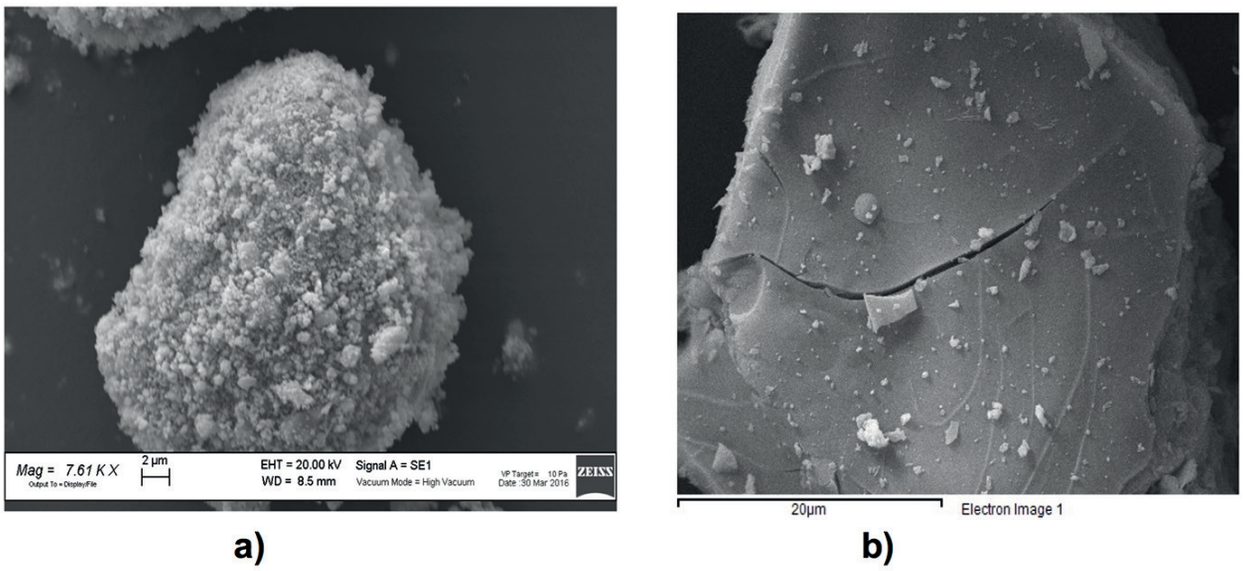

c)

Element	App Conc.	Intensity Corrn.	Weight %	Weight % Sigma	Atomic %
C K	5.40	0.1902	15.71	0.28	36.98
O K	18.73	0.5468	18.94	0.14	33.49
Fe K	60.44	0.9330	35.82	0.15	18.14
Zn K	37.05	0.8516	24.06	0.13	10.41
Gd L	8.60	0.8690	5.47	0.09	0.98
Totals			100.00		

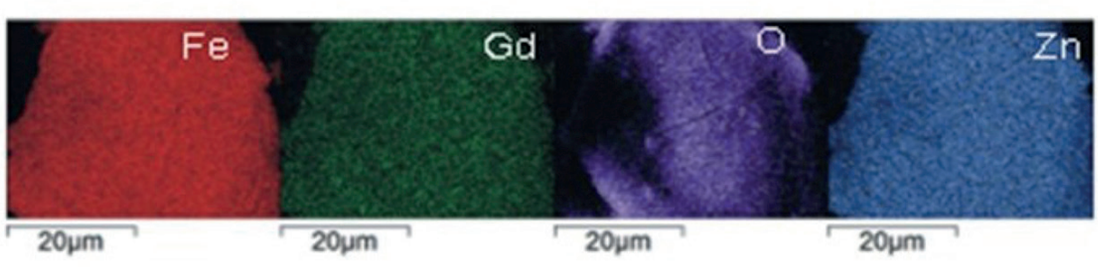

Figure 5. SEM images of Gd01 (a) and ZnFe-SS (b); data (c) and color map (d) from EDS elemental analysis for Gd01 sample.

volume ratio for MW samples with respect to solid-state one. From MW, rounded particles (lower than 100 nm) aggregates with large and open pores, regardless the doping ion, can be seen. This aspect can be due to the evolution of gases from nitrates and citric acid (such as NO_2 and CO_2) during the heating process in the microwave oven. The solid-state synthesis also leads to aggregates, but with larger rounded particles. The electronic microanalysis allowed us to verify that the stoichiometric ratio between the different elements was maintained in the final products. In **Figure 5c**, as an example, the EDS analysis of Gd01 sample is reported. The atomic percentages of all the elements are in excellent agreement with the stoichiometric values, within the EDS detection limit, suggesting that the ferrites possess the expected composition and no ions loss occurred. The maps of the different elements show good homogeneity, suggesting that Gd ions are well distributed in the sample. A similar behavior was observed for all the undoped and the other doped samples.

2.2.3. Magnetic results

Hysteresis cycles at RT and at 10 K have been measured as well as the zero-field and field cooled magnetization curves in temperature. The magnetic data have been carefully analyzed [59], and they provide a basic proof of the RT superparamagnetic behavior, essential requirement in magnetic hyperthermia. Examples for the hysteresis curves at RT and 10 K are reported in **Figure 6a** for the Ca005 sample, as well the relative ZFC and FC magnetization curves (**Figure 6b**).

The magnetic behavior for all the samples is summarized in **Table 4**, where all the functional parameters are reported.

We found, for all the MW samples, a superparamagnetic behavior with saturation magnetization at RT between 6 and 10 emu/g at the maximum applied magnetic field of 3 T, with a more effective role played by Ca ions with respect to Gd ions substitution. A fair agreement is found with the M_S values reported in the literature for pure and doped zinc ferrite spinels having comparable grain size and prepared by means of combustion synthesis or other methods [10, 60, 62–64]. In $ZnFe_2O_4$, the inversion promotes super exchange interactions, in turn

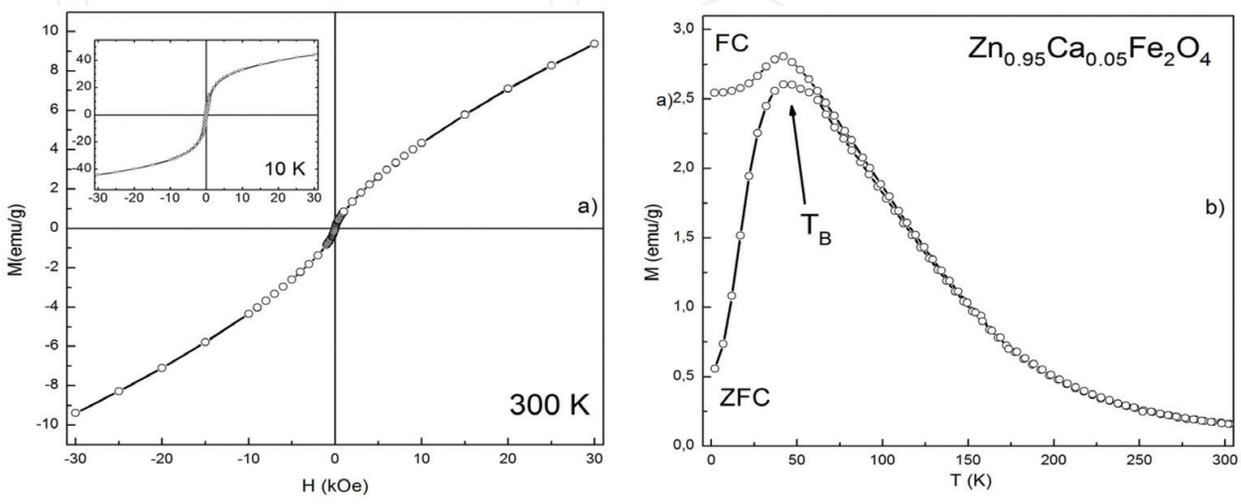

Figure 6. (a) Hysteresis loops at 300 K and at 10 K (in the inset) for Ca005; (b) ZFC and FC magnetization data for the same sample.

	T_B (K)	T_{Irr} (K)	H_C (300 K) (Oe)	M_{Rem} (300 K) (emu/g)	M_{Sat} (300 K–30 kOe) (emu/g)	H_C (10 K) (Oe)	M_{Rem} (10 K) (emu/g)	M_{Sat}(10 K–30 kOe) (emu/g)
ZnFe-SS	24	24	0	0	Linear behavior (5.3)	80	0.6	30.4
ZnFe	42	70	Negl	Negl	8.7 (S shape)	115	3.3	38.2
Al01	50	100	Negl	Negl	6.7 (S shape)	350	3.4	26.7
Ca005	45	100	Negl	Negl	10.0 (S shape)	250	5.2	45.0
Ca025	52	70	Negl	Negl	5.8 (S shape)	100	2.3	21.5
Sr005	53	85	Negl	Negl	8.1 (S shape)	90	1.6	18.2
Gd01	34	60	Negl	Negl	6.7 (S shape)	115	2.8	43.7

Table 4. Different functional parameters derived from magnetization experiments: (i) the blocking temperature, T_B, as defined in the introduction; (ii) the irreversibility temperature, T_{Irr}, corresponding to the merging of ZFC and FC curves and its distance from T_B (T_{Irr} gives suggestions about spin and structural disorder of nanoparticles also come from the temperature); (iii) coercive field H_c, remnant and saturation magnetization (M_{Rem} and M_{Sat}) both at RT and 10 K. The term negligible (Negl) means lower than 5 Oe for H_c, and lower than 10^{-2} for M_{rem}.

responsible of higher M_S values with respect to the regular spinel. Magnetization data give evidence on the effective role of inversion degree, even if M_S values correlate in a complex manner with the spinel inversion.

2.2.4. Raman results

In **Figure 7**, the Raman spectra of pure and doped MW ZFO samples are reported together with pure ZFO sample obtained by solid state synthesis.

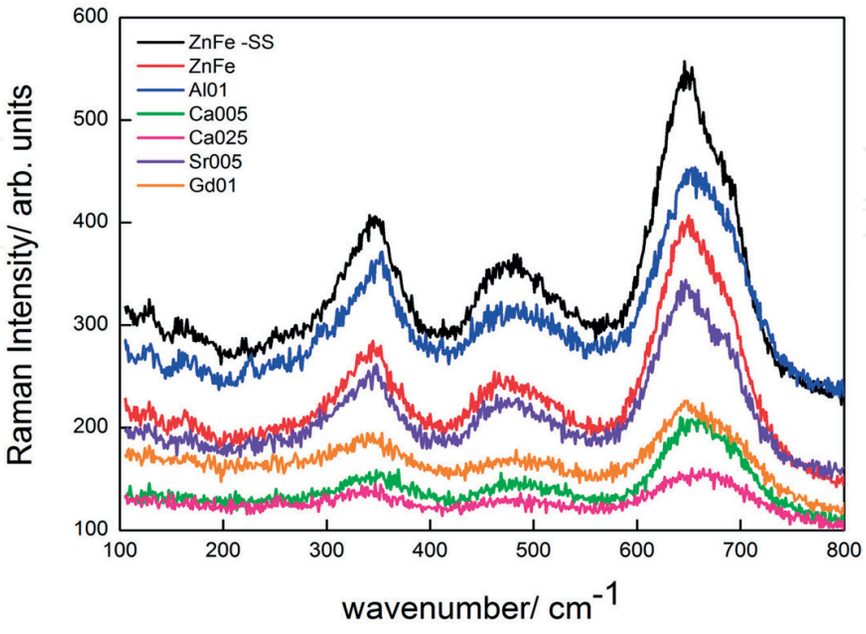

Figure 7. Raman spectra at RT in the region from 100 to 800 cm^{-1} for all the samples investigated.

For all the samples, a well-defined first order Raman scattering pertinent to the ferrite phase has been detected with the most prominent signals around 650 cm^{-1} (A_{1g} mode) accompanied by the other modes at lower energy. The substantial invariance of the Raman features for all the samples indicates a good stability of the spinel structure. The lower total Raman yield and the broadening of the signals of MW samples are consistent with the lower density and smaller crystallite size of the MW powders as derived by XRD analyses. Doping seems to play a negligible role in the peak positions, with the exception of Ca025 sample. For this heavily doped sample, the higher bands move at higher energies, while the $F_{2g}(2)$ signal further decreases in energy. For Ca and Gd samples, a weak feature at around 220 cm^{-1}, probably due to the $F_{2g}(1)$ mode, is present. By comparing the pure samples, we can notice a weak, but observable, red-shift for all the Raman features of the MW sample. This fact is compatible with the reduction of crystallite size (11 nm for ZnFe and 22.9 nm for ZnFe-SS). The peak position of A_{1g} moves from 642.5 to 638.5 cm^{-1}, while the $F_{2g}(2)$ peak is peaked at 345.0 cm^{-1} for ZnFe-SS sample and at 334.0 cm^{-1} for ZnFe one.

The lattice parameter value could play a role in this red shift. According to [44], the changes in Raman line position are related to the changes in the lattice parameter by the relationship $\Delta\omega_i = -3\,\gamma_i(q)\omega_i(q)(\Delta a/a_0)$, where γ is the Gruneisen mode parameter and $\Delta\omega_i$ is the shift of Raman line. The values of γ taken by [27] are 0.72 for A_{1g} mode and 1.88 for the F_{2g} lower energy mode. From the lattice parameters reported in **Table 3**, we derive an expected Raman shift of about 2.0 and 3.5 cm^{-1} for A_{1g} and F_{2g} modes, respectively. The measured shifts are greater and thus the lattice parameter by itself cannot account for the observed Raman softening, for which the role of inversion in the spinel structure must be considered.

As discussed in the previous section, all the Raman data in the region 200–800 cm^{-1} have been treated by best-fitting procedures. Due to the different involved masses, we used couples of oscillators for the three main Raman features with an additional curve for the low energy weaker signals. Even for higher doping levels (Al01, Gd01 and Ca025), we avoid to introduce a third oscillator. A very satisfactory agreement with experimental data has been obtained. As an example, we report the result for sample ZnFe-SS in **Figure 8**.

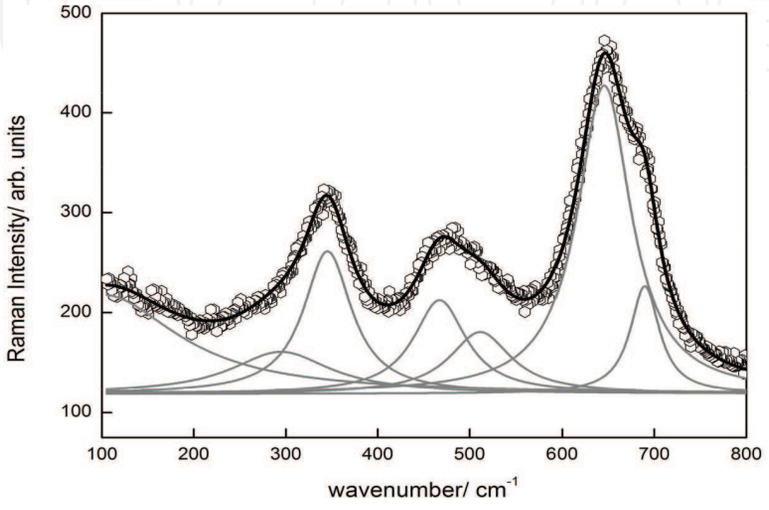

Figure 8. A representative example of best-fitting of the Raman spectrum in the range of 100–800 cm^{-1} for sample ZnFe-SS.

In particular, for the whole set of samples, the A_{1g} band is well fitted by the overlapping of two signals: the first, centered at around 641 cm^{-1}, gives the main contribution and the second, centered at around 685 cm^{-1}, results in a shoulder at higher energies. The energies are in good agreement with those expected for modes inside ZnO_4 and FeO_4 units. From the intensities of these bands, by applying the simple formula $I_{685}/(I_{685} + I_{641})$, we could estimate the inversion degree obtaining, for ZnFe-SS sample, i.e., our standard reference, a value equal to 0.095, slightly higher than 0.07, derived from XRD analysis.

The results for inversion degree are reported in **Figure 9**, where the same parameter from XRD analyses is already shown for comparison.

Even if absolute values from the two methods do not coincide, a common trend is evidenced and the highest inversion is found for Ca025 from both the techniques. Anyway, the discrepancies can be due to the different penetration depths of the two probes leading to the detection of different structural features, especially when clustered nanometric particles are involved. XRD sampling involves the bulk of the sample while Raman measurements probe mainly the surfaces, i.e., the most defective and disordered sample zones and thus it is not surprising that for undoped and low-level doped samples higher inversion degree are derived from Raman. On the contrary, for Al01 and Ca025 samples, a slightly higher inversion degree is derived from XRD analysis. In these cases, we have the higher doping level; in addition the ionic radii of Ca and Al ions are markedly higher and lower, respectively, than that of Zn and Fe ones with respect to other samples, and the differences in ionic radii with respect to the substituted ions. In fact, Ca ions are markedly greater, while Al markedly lower than Zn and Fe ones [61]. In addition, Ca025 powders exhibit the lower crystallite size. All these elements can lead to an increase of inversion degree even in the core of nanoparticles. Finally, we remark that at higher doping level, the contribution of substituents in Raman modes can give rise to a proper vibration at a specific energy. The two Lorenztian model used to interpolate A_{1g} modes remain effective even with minor physical meaning and the error in inversion degree estimation can grow.

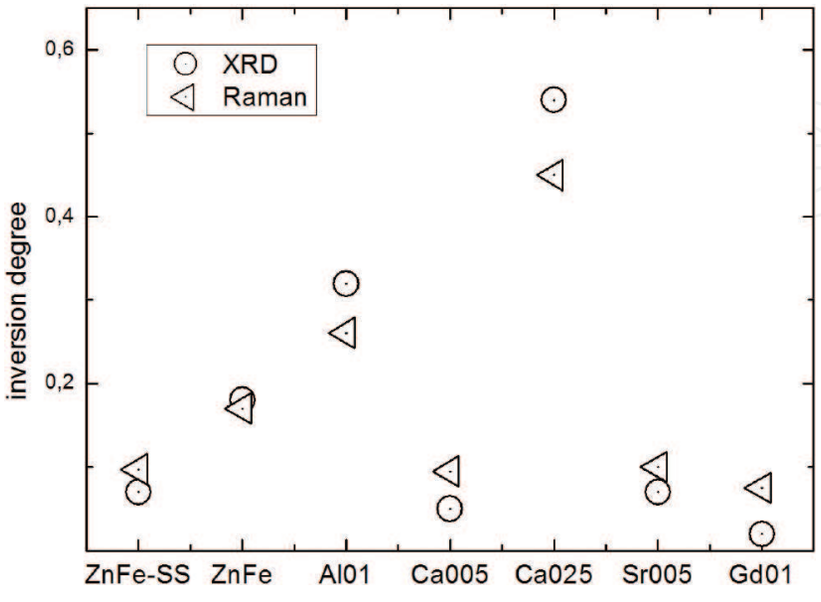

Figure 9. Inversion degree parameters obtained from Raman and XRD data as explained in the text, for all the synthesized ferrite samples. For each sample several Raman runs have been performed in different sample zones to obtain an average inversion degree with a range of variation of about 10%.

Nevertheless, it is important to underline, as evidenced in **Figure 10**, that the best-fitting procedure with two lorentzian curves allows a very good interpolation of the experimental data.

Apart from the estimation of inversion degree, from the fitting procedures the Raman band parameters have been derived for all the samples. **Figure 11** shows the integrated intensities and linewidths and allow to graphically appreciate what already observed above. A marked decrease in total Raman yield for Ca025, especially for the component peaked at 648 cm^{-1}. This component is the most affected by the substitution on A site, thus confirming the attribution for this mode.

As a final remark, one can infer that all the Raman data from MW samples indicate a good crystalline quality, absence of impurities or at least below the threshold of sensitivity, but in any case in agreement with results from XRD and morphological and chemical analyses. Thus, the magnetic functional parameters should be considered as intrinsic of the ZFO matrix, eventually doped.

Anyway, from what discussed in Section 2.1, the Raman experimental set-up allows us to evaluate the stability of the pure and doped MW ZFO powders under laser irradiation and thus to infer about the presence of cluster of maghemite. It is difficult to appreciate the presence of maghemite directly from the Raman spectra, even after detailed spectral analyses. Hence, all the samples were evaluated by means of thermal cycles. Neutral filters with optical density equal to 2, 1, 0.6, 0.3, and 0 were used leading to power density values from 5×10^3 to 5×10^5 W/cm^2. The samples were tested in different regions.

In **Figure 12a** and **b**, we report the results from the sample Al01 and the sample Sr005, respectively. These figures show two different behaviors in term of phase stability.

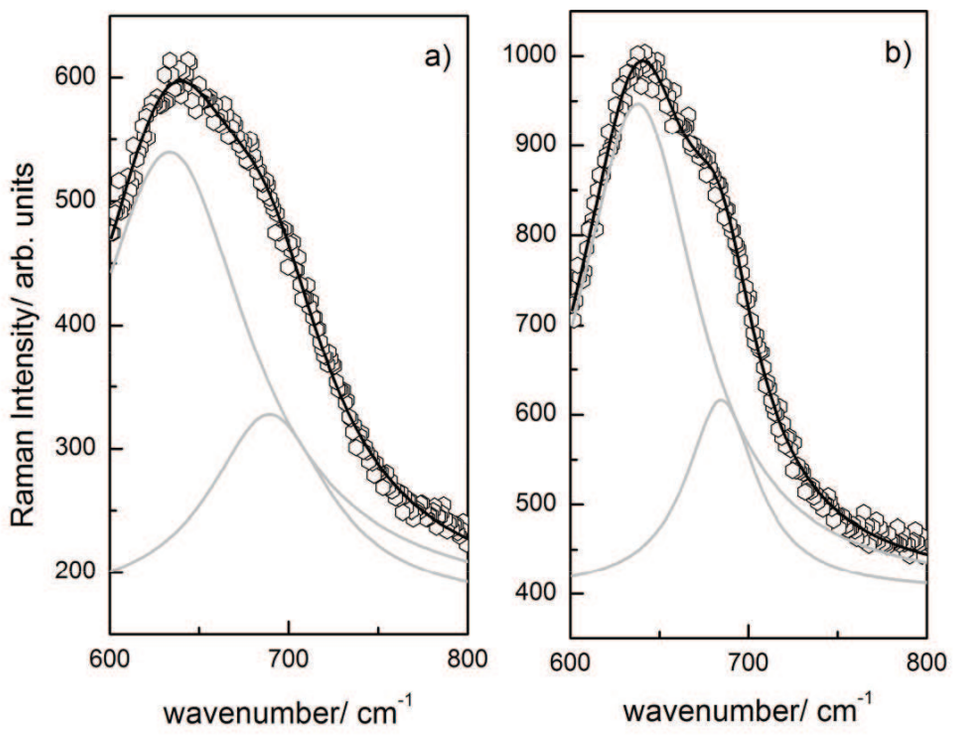

Figure 10. Raman data and curves from best-fitting runs for (a) ZnFe and (b) Sr005.

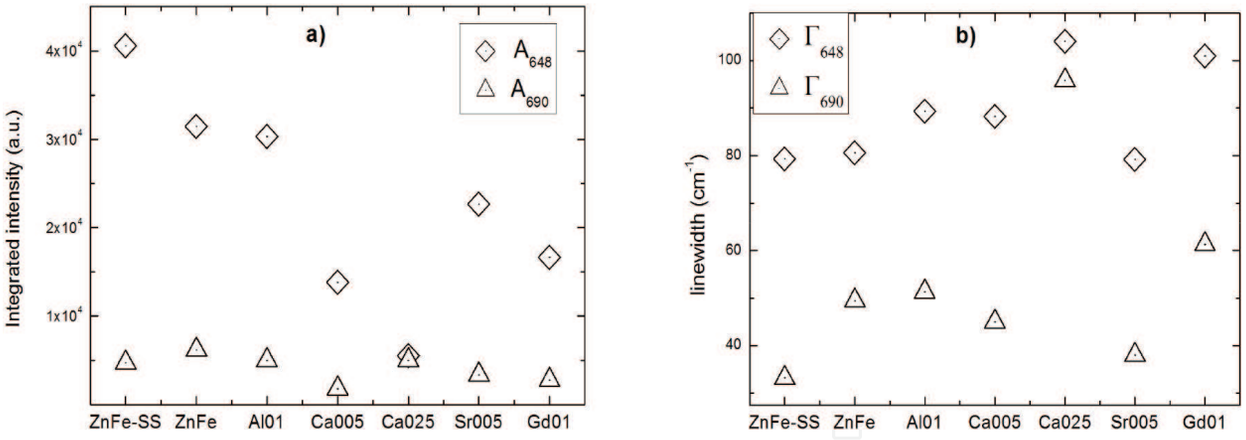

Figure 11. (a) Integrated intensities and (b) linewidths for the two lorenztian curves derived from the best fitting of A_{1g} modes for all the investigated samples.

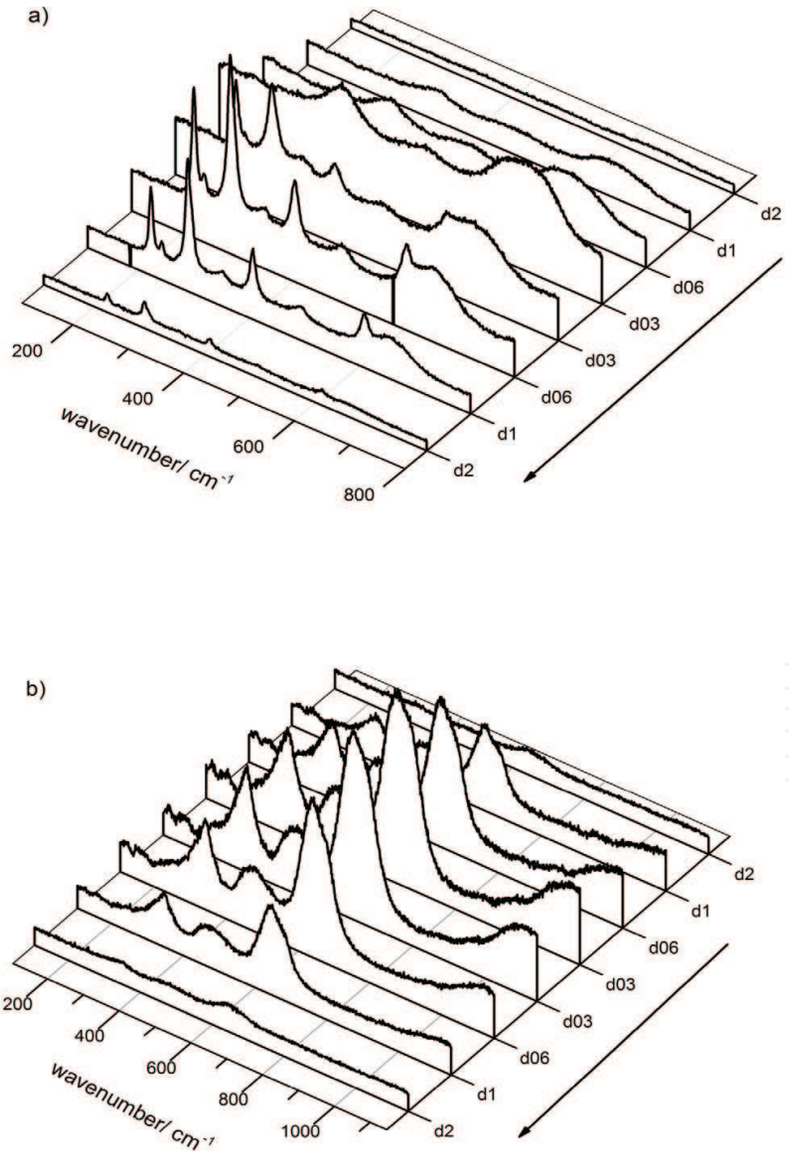

Figure 12. Raman spectra of Al01 (a) and Sr005 (b) samples collected during a thermal cycle. The samples were irradiated for 5 min and then measured at the selected power density.

The sample Sr005, even if thermally treated under laser light, remains stable showing the same Raman spectrum during the whole laser-induced thermal cycle. Small peak shifts are due to temperature effects on lattice parameters. On the contrary for Al01 sample, it is evident that upon irradiation, the Raman spectrum of the Al01 change markedly and the typical Raman features of hematite appear when the sample is maintained under laser light having a power density equal to 2×10^5 W/cm^2. When the laser light is attenuated at the end of the thermal cycle, the signal of hematite is still observable indicating a stable conversion. This is an indirect proof that at the beginning of the thermal cycle nanoregions in the irradiated volume had a structure different from the proper ZFO structure. It is likely that nanoregions of maghemite or highly defective Zn deficient zinc ferrite layers were present. We underline that the grain sizes for Al01 and Sr005 are similar.

Only three samples exhibit a stable pure zinc ferrite phase with no hematite detected at the end of the thermal cycle: ZnFe-SS, Ca025, and Sr005. The first exhibited a paramagnetic behavior, while the latter were found to be superparamagnetic. The phase stability proved by monitoring the Raman spectrum under laser heating is fundamental to validate the quality of the powders with good magnetic functional parameters, in particular in view of applications in biomedical field.

3. Conclusions and outlook

This chapter gave a look on the potential of Raman spectroscopy when applied to nanosized zinc ferrites. The nanostructured spinel $ZnFe_2O_4$ display a peculiar mixing of high-quality functional properties, and it is used in magnetic storage, ferrofluids, catalysis, and biomedical applications, as for instance theranostics and hyperthermia. For the latter applications, a strong requirement is the superparamagnetic behavior at RT, which take place in zinc ferrites thanks to the nanometric scaling. This behavior has been revealed even in pure ZFO nanoparticles due to the inversion between divalent and trivalent cations on the tetrahedral and octahedral sites of the spinel-type structure. In this frame, thanks to its intrinsic sensitivity to chemical and structural composition, Raman spectroscopy has been widely used to monitor cations distribution in pure and doped zinc ferrites. In the first part of the chapter, the state of the art concerning the results from Raman scattering in pure and doped zinc ferrites has been presented in connection to the different synthesis methods employed to obtain high quality nanostructured ferrites. It appears clear how detailed analyses on Raman data allow to evaluate the influence of nanometric scaling on Raman lines features—peak energies, widths and shape, to obtain information on the inversion degree, to reveal the presence of extrinsic iron oxides phases like hematite or magnetite and to monitor stability of spinel ferrites vs. light exposure or thermal treatment. This information is essential to assess the functional quality of the materials and it is essential to study and understand the close correlation between functional parameters and morphology, gran size, intentional doping, cation distribution, and nanoparticle architecture. Indeed magnetic, structural and chemical purity and homogeneity of nanoparticles must be thoroughly verified because even low amount of extrinsic phases can alter the functional properties. Indeed, low amount of hematite or maghemite can alter the long-term stability of nanoparticles especially in biological environment, favoring aggregation.

In the second part of the chapter, we presented original results from room temperature micro-Raman studies on nanostructured undoped $ZnFe_2O_4$, $Zn_{1-x}Ca_xFe_2O_4$ (x = 0.05 and 0.25), $ZnFe_{1.9}Gd_{0.1}O_4$, $Zn_{0.95}Sr_{0.05}Fe_2O_4$, and $ZnFe_{1.9}Al_{0.1}O_4$ doped ferrites. The samples have been prepared by using the microwave-assisted combustion method, a rapid, green, and simple synthesis route, able to ensure good physical and chemical properties. We underline the relevance of Ca substitution due to the low toxicity of the substituent; on the other side, Gd doping is rarely reported in zinc ferrites. Raman experiments have been accompanied by detailed analyses on morphological, compositional, structural, and magnetic characterization. Thus, results from XRD, SEM-EDS are briefly presented as well as the magnetic behavior. A detailed analysis of A_{1g}, E_g, $3F_{2g}$ Raman modes has been performed and Raman band parameters have been derived from best-fitting procedures and carefully compared to literature data. The results have been discussed in relation with grain size, inversion degree and doping of zinc ferrite spinel. An optimum purity level and homogeneity and crystallite sizes lower than 11 nm were determined for the doped samples. The inversion degree of the different samples was derived by both Raman and XRD data and a well agreement has been observed. The superparamagnetism seems to be favored in Ca doped samples, while in Gd doped one it is almost negligible. This is clearly associated to the inversion induced by the doping in the tetrahedral site. In addition by Raman studies we evaluated the stability of pure and doped $ZnFe_2O_4$ with laser heating just to reveal the presence of maghemite in the samples. This set of data gives evidence to the ability of Raman spectroscopy in a typical problem of solid-state material science. Finally, the present results will be the bases of further works aimed to exploit SERS effect using non-metallic nanostructured zinc ferrites eventually functionalized for specific biomedical applications.

Author details

Pietro Galinetto[1]*, Benedetta Albini[1], Marcella Bini[2] and Maria Cristina Mozzati[1]

*Address all correspondence to: pietro.galinetto@unipv.it

1 Department of Physics and CNISM, University of Pavia, Pavia, Italy

2 Department of Chemistry, University of Pavia, Pavia, Italy

References

[1] Kmita A, Pribulova A, Holtzer M, Futas P, Roczniak A. Use of specific properties of zinc ferrite in innovative technology. Archives of Metallurgy and Materials. 2016;**61**(4):2141-2146. DOI: 10.1515/amm-2016-0289

[2] Suchomski C, Breitung B, Witte R, Knapp M, Bauer S, Baumbach T, Reitz C, Brezesinski T. Microwave synthesis of high-quality and uniform 4 nm $ZnFe_2O_4$ nanocrystals for application in energy storage and nanomagnetics. Beilstein Journal of Nanotechnology. 2016; **7**:1350-1360. DOI: 10.3762/bjnano.7.126

[3] Goutham S, Kumar DS, Sadasivuni KK, Cabibihan JJ, Rao KV. Nanostructure $ZnFe_2O_4$ with *Bacillus subtilis* for detection of LPG at low temperature. Journal of Electronic Materials. 2017;**46**(4). DOI: 10.1007/s11664-016-5273-z

[4] Mady AH, Baynosa ML, Tuma D, Shim JJ. Facile microwave-assisted green synthesis of Ag-$ZnFe_2O_4$@rGO nanocomposites for efficient removal of organic dyes under UV- and visible-light irradiation. Applied Catalysis B: Environmental. 2017;**203**:416-427

[5] Díaz-Pardo R, Valenzuela R. Characterization of magnetic phases in nanostructured ferrites by electron spin resonance. In: Bashir R, editor. Advanced Electromagnetic Waves. Rijecka: InTech; 2015. DOI: 10.5772/61508. Available from: https://www.intechopen.com/books/advanced-electromagnetic-waves/characterization-of-magnetic-phases-in-nanostructured-ferrites-by-electron-spin-resonance

[6] Sheikh A, Jain P. A thorough study of zinc ferrite nanoparticles with reference to green synthesis. International Journal of Nanomedicine. 2016;**2**(3). DOI: 10.16966/2470-3206.115

[7] Issa B, Obaidat IM, Albiss BA, Haik Y. Magnetic nanoparticles: Surface effects and properties related to biomedicine applications. International Journal of Molecular Sciences. 2013;**14**:21266-21305. DOI: 10.3390/ijms141121266

[8] Kolhatkar AG, Jamison AC, Litvinov D, Willson RC, Randall Lee T. Tuning the magnetic properties of nanoparticles. International Journal of Molecular Sciences. 2013;**14**:15977-16009. DOI: 10.3390/ijms140815977

[9] Štefanić G, Krehula S, Štefanić I. Phase development during high-energy ball-milling of zinc oxide and iron – The impact of grain size on the source and the degree of contamination. Dalton Transactions. 2015;**44**:18870. DOI: 10.1039/c5dt02498f

[10] Manikandan A, Vijaya JJ, Kennedy LJ, Bououdina M. Microwave combustion synthesis, structural, optical and magnetic properties of $Zn_{1-x}Sr_xFe_2O_4$ nanoparticles. Ceramics International. 2013;**39**:5909-5917. DOI: 10.1016/j.ceramint.2013.01.012

[11] Lima-Tenório MK, Oliveira LAS, Guilherme MR, Tenório-Neto ET, Silva MF, Fernandes DM, Hechenleitner AAW, Pineda EAG. Tuning the magnetic properties of ferrite nanoparticles by Zn and Co doping. Materials Letters. 2017;**195**:151-155. DOI: 10.1016/j.matlet.2017.02.122

[12] Diodati S, Pandolfo L, Caneschi A, Gialanella S, Gross S. Green and low temperature synthesis of nanocrystalline transition metal ferrites by simple wet chemistry routes. Nano Research. 2014;**7**(7):1027-1042. DOI: 10.1007/s12274-014-0466-3

[13] Patil SB, Bhojya Naik HS, Nagaraju G, Viswanath R, Rashmi SK. Synthesis of visible light active Gd^{3+}-substituted $ZnFe_2O_4$ nanoparticles for photocatalytic and antibacterial activities. The European Physical Journal Plus. 2017;**132**:328. DOI: 10.1140/epjp/i2017-11602-x

[14] Phumying S, Labuayai S, Swatsitang E, Amornkitbamrung V, Maensiri S. Nanocrystalline spinel ferrite (MFe_2O_4, M = Ni, Co, Mn, Mg, Zn) powders prepared by a simple aloe vera plant-extracted solution hydrothermal route. Materials Research Bulletin. 2013;**48**:2060-2065. DOI: 10.1016/j.materresbull.2013.02.042

[15] Kombaiah K, Vijaya JJ, Kennedy LJ, Bououdina M. Studies on the microwave assisted and conventional combustion synthesis of Hibiscus rosasinensis plant extract based $ZnFe_2O_4$ nanoparticles and their optical and magnetic properties. Ceramics International. 2016;**42**:2741-2749. DOI: 10.1016/j.ceramint.2015.11.003

[16] Sivakumar M, Towata A, Yasui K, Tuziuti T, Iida Y. A new ultrasonic cavitation approach for the synthesis of zinc ferrite nanocrystals. Current Applied Physics. 2006;**6**:591-593. DOI: 10.1016/j.cap.2005.11.068

[17] Mohai I, Gál L, Szépvölgyi J, Gubicza J, Farkas Z. Synthesis of nanosized zinc ferrites from liquid precursors in RF thermal plasma reactor. Journal of the European Ceramic Society. 2007;**27**:941-945. DOI: 10.1016/j.jeurceramsoc.2006.04.128

[18] Ali A, Zafar H, Zia M, ul Haq I, Rehman Phull A, Sarfraz Ali J, Hussain A. Synthesis, characterization, applications, and challenges of iron oxide nanoparticles. Nanotechnology, Science and Applications. 2016;**9**:49-67. DOI: 10.2147/NSA.S99986

[19] D'Ippolito V, Andreozzi GB, Bersani D, Lottici PP. Raman fingerprint of chromate, aluminate and ferrite spinels. Journal of Raman Specroscopy. 2015;**46**:1255-1264. DOI: 10.1002/jrs.4764

[20] Chandramohan P, Srinivasan MP, Velmurugan S, Narasimhan SV. Cation distribution and particle size effect on Raman spectrum of $CoFe_2O_4$. Journal of Solid State Chemistry. 2011;**184**:89-96. DOI: 10.1016/j.jssc.2010.10.01

[21] de Faria DLA, Venaüncio Silva S, de Oliveira MT. Raman microspectroscopy of some iron oxides and oxyhydroxides. Journal of Raman Spectroscopy. 1997;**28**:873-878

[22] Singh JP, Srivastava RC, Agrawala HM, Kumarb R. Micro-Raman investigation of nanosized zinc ferrite: Effect of crystallite size and fluence of irradiation. Journal of Raman Specroscopy. 2011. DOI: 10.1002/jrs.2902

[23] Varshney D, Verma K, Kumar A. Structural and vibrational properties of $Zn_xMn_{1-x}Fe_2O_4$ (x = 0.0, 0.25, 0.50, 0.75, 1.0) mixed ferrites. Materials Chemistry and Physics. 2011;**131**:413-419. DOI: 10.1016/j.matchemphys.2011.09.066

[24] Song D, Yang R, Wang C, Xiao R, Long F. Reusable nanosilver-coated magnetic particles for ultrasensitive SERS-based detection of malachite green in water samples. Scientific Reports. 2016;**6**:22870. DOI: 10.1038/srep22870

[25] White WB, DeAngelis BA. Interpretation of the vibrational spectra of spinels. Spectrochimica Acta. 1967;**23A**:985-995. DOI: 10.1016/0584-8539(67)80023-0

[26] Hosterman BD. Raman spectroscopic study of solid solution spinel oxides [UNLV Theses, Dissertations, Professional Papers, and Capstones]. Graduate College University of Nevada: Las Vegas; 2011. p. 1087

[27] Wang Z, Schiferl D, Zhao Y, O'Neill HSC. High pressure Raman spectroscopy of spinel-type ferrite $ZnFe_2O_4$. Journal of Physics and Chemistry of Solids. 2003;**64**:2517-2523. DOI: 10.1016/j.jpcs.2003.08.005

[28] Yamanaka T, Ishii M. Raman scattering and lattice vibrations of Ni_2SiO_4 spinel at elevated temperature. Physics and Chemistry of Minerals. 1986;**13**:156-160. DOI: 10.1007/BF00308157

[29] Cynn H, Sharma SK, Cooney TF, Nicol M. High-temperature Raman investigation of order-disorder behavior in the $MgAl_2O_4$ spinel. Physical Review B. 1992;**45**(1):500-502. DOI: 10.1103/PhysRevB.45.500

[30] Larry Verble J. Temperature-dependent light-scattering studies of the Verwey transition and electronic disorder in magnetite. Physical Review B. 1974;**9**(12):5236-5248. DOI: 10.1103/PhysRevB.9.5236

[31] Julien CM, Massot M. Lattice vibrations of materials for lithium rechargeable batteries I. Lithium manganese oxide spinel. Materials Science and Engineering B. 2003;**97**:217-230. DOI: 10.1016/S0921-5107(02)00582-2

[32] Bruesch P, D'Ambrogio F. Lattice dynamics and magnetic ordering in the chalcogenide spinels $CdCr_2S_4$ and $CdCr_2Se_4$. Physica Status Solidi B. 1972;**50**:513-526. DOI: 10.1002/pssb.2220500212

[33] O'Horo MP, Frisillo AL, White WB. Lattice vibrations of $MgAl_2O_4$ spinel. Journal of Physics and Chemistry of Solids. 1973;**34**:23-28. DOI: 10.1016/0022-3697(73)90058-9

[34] Preudhomme J, Tarte P. Infrared studies of spinels III: The normal II-III spinels. Spectrochimica Acta. 1971;**27A**:1817-1835. DOI: 10.1016/0584-8539(71)80235-0

[35] Lazarević ZŽ, Jovalekić Č, Ivanovski VN, Rečnik A, Milutinović A, Cekić B, Romčević NŽ. Characterization of partially inverse spinel $ZnFe_2O_4$ with high saturation magnetization synthesized via soft mechanochemically assisted route. Journal of Physics and Chemistry of Solids. 2014;**75**:869-877. DOI: 10.1016/j.jpcs.2014.03.004

[36] Milutinović A, Lazarević Z, Jovalekić Č, Kuryliszyn-Kudelska I, Romčević M, Kostić S, Romčević N. The cation inversion and magnetization in nanopowder zinc ferrite obtained by soft mechanochemical processing. Materials Research Bulletin. 2013;**48**:4759-4768. DOI: 10.1016/j.materresbull.2013.08.020

[37] Yadav RS, Kuřitka I, Vilcakova J, Urbánek P, Machovsky M, Masař M, Holek M. Structural, magnetic, optical, dielectric, electrical and modulus spectroscopic characteristics of $ZnFe_2O_4$ spinel ferrite nanoparticles synthesized via honey-mediated sol-gel combustion method. Journal of Physics and Chemistry of Solids. 2017;**110**:87-99. DOI: 10.1016/j.jpcs.2017.05.029

[38] ZŽ Lazarević DL, Sekulić VN, Ivanovski NŽ, Romčević A. Structural and magnetic investigation of the inversion degree in spinel $NiFe_2O_4$, $ZnFe_2O_4$ and $Ni_{0.5}Zn_{0.5}Fe_2O_4$ ferrites prepared by soft mechanochemical synthesis. International Journal of Chemical, Molecular, Nuclear, Materials and Metallurgical Engineering. 2015;**9**(8)

[39] Virumbrales-del Olmo M, Delgado-Cabello A, Andrada-Chacón A, Sánchez-Benítez J, Urones-Garrote E, Blanco-Gutiérrez V, Torralvo MJ, Sáez-Puchea R. Effect of composition and coating on the interparticle interactions and magnetic hardness of MFe_2O_4

(M = Fe, co, Zn) nanoparticles. Physical Chemistry Chemical Physics. 2017;**19**:8363. DOI: 10.1039/c6cp08743d

[40] Thota S, Kashyap SC, Sharma SK, Reddy VR. MicroRaman, Mossbauer and magnetic studies of manganese substituted zinc ferrite nanoparticles: Role of Mn. Journal of Physics and Chemistry of Solids. 2016;**91**:136-144. DOI: 10.1016/j.jpcs.2015.12.013

[41] Milanović M, Stijepović I, Pavlović V, Srdić VV. Functionalization of zinc ferrite nanoparticles: Influence of modification procedure on colloidal stability. Processing and Application of Ceramics. 2016;**10**(4):287-293. DOI: 10.2298/PAC1604287M

[42] Masoudpanah SM, Hasheminisari M, Ghasemi A. Magnetic properties and photocatalytic activity of $ZnFe_{2-x}La_xO_4$ nanoparticles synthesized by sol–gel autocombustion method. Journal of Sol-Gel Science and Technology. 2016;**80**:487-494. DOI: 10.1007/s10971-016-4101-5

[43] Murugesan C, Chandrasekaran G. Structural and magnetic properties of $Mn_{1-x}Zn_xFe_2O_4$ ferrite nanoparticles. Journal of Superconductivity and Novel Magnetism. 2016;**29**:2887-2897. DOI: 10.1007/s10948-016-3604-1

[44] Spanier JE, Robinson RD, Zhang F, Chan SW, Herman IP. Size-dependent properties of CeO_2-y nanoparticles as studied by Raman scattering. Physical Review B. 2001;**64**:245407. DOI: 10.1103/PhysRevB.64.245407

[45] Arora AK, Rajalakshmi M, Ravindran TR, Sivasubramanian V. Raman spectroscopy of optical phonon confinement in nanostructured materials. Journal of Raman Spectroscopy. 2007;**38**(6). DOI: 10.1002/jrs.1684

[46] Freire RM, Ribeiro TS, Vasconcelos IF, Denardin JC, Barros EB, Mele G, Carbone L, Mazzetto SE, Fechine PBA. $MZnFe_2O_4$ (M = Ni, Mn) cubic superparamagnetic nanoparticles obtained by hydrothermal synthesis. Journal of Nanoparticle Research. 2013;**15**:1616. DOI: 10.1007/s11051-013-1616-3

[47] Lazarević ZŽ, Milutinović AN, Jovalekić ČD, Ivanovski VN, Daneu d N, Maparević I, Romĉević NŽ. Spectroscopy investigation of nanostructured nickel–zinc ferrite obtained by mechanochemical synthesis. Materials Research Bulletin. 2015;**63**:239-247. DOI: 10.1016/j.materresbull.2014.12.005

[48] Thota S, Kashyapa SC, Sharmab SK, Reddyca VR. Cation distribution in Ni-substituted $Mn_{0.5}Zn_{0.5}Fe_2O_4$ nanoparticles: A Raman, Mössbauer, X-ray diffraction and electron spectroscopy study. Materials Science and Engineering B. 2016;**206**:69-78. DOI: 10.1016/j.mseb.2016.01.002

[49] Varshney D, Verma K, Kumar A. Substitutional effect on structural and magnetic properties of $A_xCo_{1-x}Fe_2O_4$ (A = Zn, Mg and x = 0.0, 0.5) ferrites. Journal of Molecular Structure. 2011;**1006**:447-452. DOI: 10.1016/j.molstruc.2011.09.047

[50] Jovanovic S, Spreitzer M, Tramsek M, Trontelj Z, Suvorov D. Effect of oleic acid concentration on the physicochemical properties of cobalt ferrite nanoparticles. Journal of Physical Chemistry C. 2014;**18**:13844-13856. DOI: 10.1021/jp500578f

[51] da Silva SW, Nakagomi F, Silva MS, Franco A Jr, Garg VK, Oliveira AC, Morais PC. Raman study of cations' distribution in $Zn_xMg_{1-x}Fe_2O_4$ nanoparticles. Journal of Nanoparticle Research. 2012;**14**:798. DOI: 10.1007/s11051-012-0798-4

[52] Chaudhari PR, Gaikwad VM, Acharya SA. Role of mode of heating on the synthesis of nanocrystalline zinc ferrite. Applied Nanoscience. 2015;**5**:711-717. DOI: 10.1007/s13204-014-0367-5

[53] Liua J, Denga M, Huanga Z, Yina G, Liaoa X, Gub J. Preparation of $ZnFe_2O_4$ nanoparticles in the template of silk-fibroin peptide and their neuro-cytocompability in PC12 cells. Colloids and Surfaces B: Biointerfaces. 2013;**107**:19-26. DOI: 10.1016/j.colsurfb.2013.01.072

[54] Malavasi L, Galinetto P, Mozzati MC, Azzoni CB, Flor G. Raman spectroscopy of AMn_2O_4 (A = Mn, Mg and Zn) spinels. Physical Chemistry Chemical Physics. 2002;**4**:3876-3880. DOI: 10.1039/B203520K

[55] Thomas JJ, Shinde AB, Krishna PSR, Kalarikkal N. Temperature dependent neutron diffraction and Mossbauer studies in zinc ferrite nanoparticles. Materials Research Bulletin. 2013;**48**:1506-1511. DOI: 10.1016/j.materresbull.2012.12.058

[56] Gomes JA, Azevedo GM, Depeyrot J, Mestnik-Filho J, Paula FLO, Tourinho FA, Perzynski R. Structural, chemical, and magnetic investigations of core-shell zinc ferrite nanoparticles. Journal of Physical Chemistry C. 2012;**116**:24281-24291. DOI: 10.1021/jp3055069

[57] Chernyshova IV, Hochella MF, Madden AS. Size-dependent structural transformations of hematite nanoparticles.1.Phase transition. Physical Chemistry Chemical Physics. 2007;**9**:1736-1750. DOI: 10.1039/B618790K

[58] Galinetto P, Mozzati MC, Grandi MS, Bini M, Capsoni D, Ferrari S, Massarotti V. Phase stability and homogeneity in undoped and Mn-doped $LiFePO_4$ under laser heating. Journal of Raman Spectroscopy. 2010;**41**:1276-1282. DOI: 10.1002/jrs.2558

[59] Bini M, Tondo C, Capsoni D, Mozzati MC, Albini B, Galinetto P. Superparamagnetic $ZnFe_2O_4$ nanoparticles: The effect of Ca and Gd doping. Materials Chemistry and Physics. 2018;**204**:72-82. DOI: 10.1016/j.matchemphys.2017.10.033

[60] Tholkappiyan R, Vishista K. Influence of lanthanum on the optomagnetic properties of zinc ferrite prepared by combustion method. Physica B. 2014;**448**:177. DOI: 10.1016/j.physb.2014.04.022

[61] Shannon RD. Revised effective ionic radii and systematic studies of interatomic distances in halides and chalcogenides. Acta Cryst. 1976;**A32**:751-767. DOI: 10.1107/S0567739476001551

[62] Yadav RS, Havlica J, Kuritka I, Kozakova Z, Palou M, Bartonıckova E, Bohac M, Frajkorova F, Masilko J, Hajduchova M, Enev V, Wasserbauer J. Magnetic properties of $ZnFe_2O_4$ nanoparticles synthesized by starch-assisted sol-gel auto-combustion method. Journal of Superconductivity and Novel Magnetism. 2015;**28**:1417. DOI: 10.1007/s10948-014-2870-z

[63] Milanovic M, Moshopoulou EG, Stamopoulos D, Devlin E, Giannakopoulos KP, Kontos AG, Eleftheriadis K, Gini MI, Nikolic LM. Structure and magnetic properties of $Zn_{1-x}In_xFe_2O_4$ and $ZnY_xFe_{2-x}O_4$ nanoparticles prepared by coprecipitation. Ceramics International. 2013;**39**:3235. DOI: 10.1016/j.ceramint.2012.10.011

[64] Roy MK, Halder B, Verma HC. Characteristic length scales of nanosize zinc ferrite. Nanotechnology. 2006;**17**:232. DOI: 10.1088/0957-4484/17/1/039

IntechOpen

IntechOpen